Peer-reviewed version available at *Nanomaterials* **2017**, *7*, , 121; doi:10.3390/nano7060121

Fast Preparation of Porous MnO/C Microspheres as Anode Materials for Lithium-Ion Batteries

Jing Su[a,c], Hao Liang[a], Xian-Nian Gong[a], Xiao-Yan Lv [b], Yun-Fei Long[a] and Yan-Xuan Wen[a,c,*]

[a]School of Chemistry and Chemical Engineering, Guangxi University, Nanning 530004, China; sujing928@126.com (J.S.); 15253732337@163.com (H.L.); 138786083682050@163.com (X.-N.G.); longyf@gxu.edu.cn (Y.-F.L.)

[b]Guangxi Colleges and Universities Key Laboratory of Novel Energy Materials and Related Technology, Nanning 530004, China; lvxiaoyan666@163.com

[c]The New Rural Development Research Institute, Guangxi University, Nanning 530004, China

*Correspondence: wenyanxuan@vip.163.com; Tel:+86-771-3233718; Fax: +86-771-3233718

ABSTRACT

Porous MnO/C microspheres have been successfully fabricated by a fast co-precipitation method in a T-shaped microchannel reactor. The structures, compositions and electrochemical performances of the obtained MnO/C microspheres are characterized by X-ray diffraction, emission scanning electron microscopy, transmission electron microscopy (HRTEM), Brunauer–Emmett–Teller analysis, charge-discharge testing, cyclic voltammograms, and electrochemical impedance spectra. Experimental results reveal that the as-prepared MnO/C, with a specific surface area of 96.66 $m^2 \cdot g^{-1}$ and average pore size of 24.37 nm, exhibits excellent electrochemical performance, with a discharge capacity of

Peer-reviewed version available at Nanomaterials 2017, 7, , 121; doi:10.3390/nano7060121

655.4 mAh·g^{-1} after cycling 50 times at 1 C and capacities of 808.3, 743.7, 642.6, 450.1, and 803.1 mAh·g^{-1} at 0.2, 0.5, 1, 2, and 0.2 C, respectively. Moreover, the controlled method of using a micro-channel reactor, which can produce larger specific surface area porous MnO/C with improved cycling performance by shortening lithium-ion diffusion distances, can be easily applied in real production on a large-scale.

Keywords: lithium-ion batteries; anode materials; MnO; co-precipitation; T-shaped microchannel reactor

1. Introduction

In the past few decades, rechargeable lithium-ion batteries (LIBs) have attracted considerable attention as the major power source for portable electronic devices and electric vehicles [1–3]. However, the commercial anode material, graphite, is difficult to meet the increasing demand for large energy and power densities with a limited theoretical capacity of 372 mAh·g^{-1} [4, 5]. Transition metal oxides have attracted significant research attention due to their two or three times improved reversible capacity when compared with graphite [6–8]. Among all the kinds of transition metal oxides investigated for LIBs, manganese oxide (MnO) has received particular interest because of its high theoretical capacity (755 mAh·g^{-1}), relatively low electromotive force (1.032 V *vs.* Li$^+$/Li),

Peer-reviewed version available at Nanomaterials 2017, 7, , 121; doi:10.3390/nano7060121

high density (5.43 $g \cdot cm^{-3}$), environmental friendliness and abundance in nature [9–11]. However, poor cycling stability and rate capability, owing to the low conductivity and large volume changes during Li-ion insertion/extraction, have hampered the application of MnO [12, 13]. Many strategies have been adopted to overcome these shortcomings, such as downsizing the particle size [14, 15], designing new morphologies [16, 17], doping [18–22], carbon coating [23–27], and constructing hollow or porous structures [28–33].

Among all these strategies, structuring porous MnO electrodes has been an effective strategy for enhancing the capacity retention by reversibly accommodating large volume changes. And the pores of the porous electrode provide good access for the electrolyte to the electrode surface. The large surface areas of the porous structures also facilitate charge transfer across the electrode/electrolyte interfaces[34].

Porous MnO materials can be synthesized by templated or non-templated methods, such as co-precipitation[35], hydrothermal, solvothermal[36], sol-gel and deposition processes[37]. Among these synthesis method, The co-precipitation method is more simple than the above mentioned processes and is suitable for large-scale production in commercial fields. Zhong et al. [35] synthesized porous MnO/C microspheres which delivered a reversible capacity of 600 $mAh \cdot g^{-1}$ at a rate of 400 $mA \cdot g^{-1}$. This porous MnO particles were obtained with

$MnCO_3$ as the precursor through a co-precipitation method, and carbon was coated by chemical vapor deposition. However, the particle size and distribution from the co-precipitation method always depend on the mass transfer and dispersion in the reactor. In traditional co-precipitation, solutions are mixed by stirring for several honrs [9, 35], which is not easy to control the particle nucleation-growth processes. It is necessary to improve the micro-mixing intensity and mass transfer for the co-precipitation process.

In this article, a noval and simple method for the fast synthesis of porous MnO/C microspheres with large specific areas was demonstrated for the first time. $MnCO_3$ precursor was preperated in a T-shaped microchannel reactor only for a few seconds. Due to the enhancement of mixing effect in the microchannel reactor, the MnO/C microspheres were with narrow size distribution and improved electrochemical performance[38, 39].

2. Experimental

2.1. Preparation of Materials

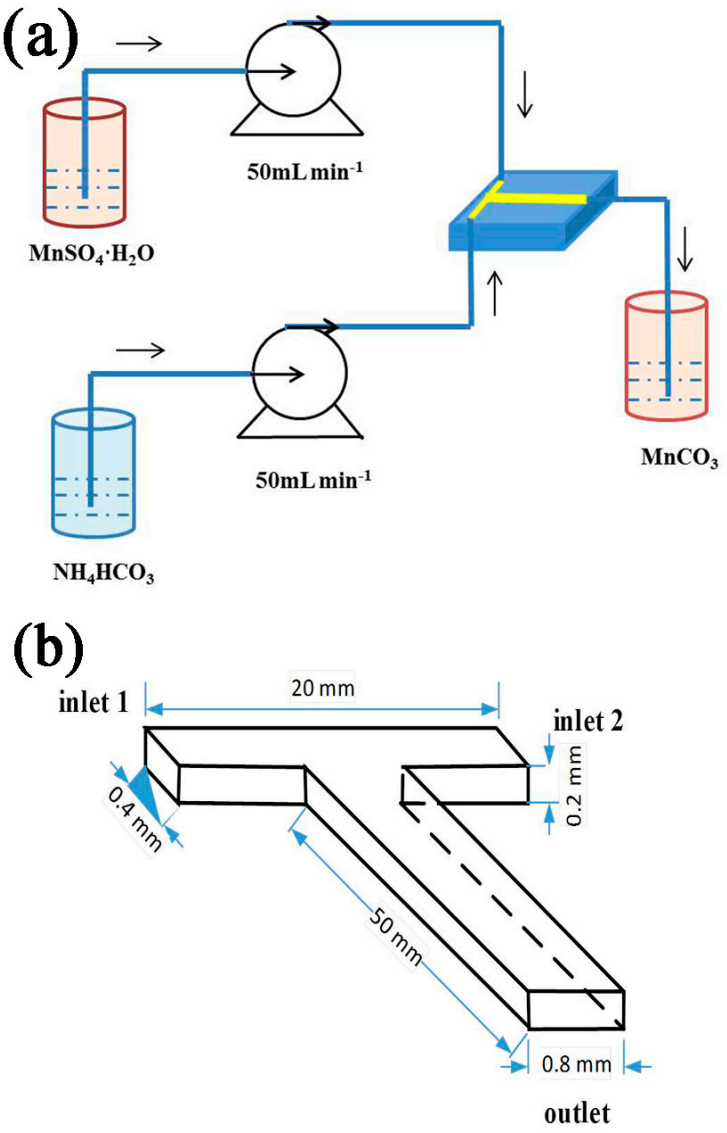

Fig. 1. The experimental setup for the preparation of $MnCO_3$ (a) and the sketch of the T-shaped microchannel reactor (b).

Porous MnO/C was prepared as follows. Two solutions of $MnSO_4 \cdot H_2O$ (0.1 $mol \cdot L^{-1}$) and NH_4HCO_3 (0.2 $mol \cdot L^{-1}$) were simultaneously injected into the T-shaped microchannel reactor with an accurate syringe pump (2PB00C, Beijing Xingda Technology Co.,Ltd.,China) at the same fixed

flow rate of 50 mL·min^{-1} to generate the crystal $MnCO_3$ (Fig. 1(a)). Following this co-precipitation process, the product was collected by filtration, washed out the sulfate ion (tested the washing water with a 0.5 mol·L^{-1} $BaCl_2$ solution) and dried in a vacuum oven at 60 °C. After that, the synthesized $MnCO_3$ precursor was mixed with sucrose at a mass ratio of 10:3 by ultrasonication and dried at 60 °C. Finally, the composite was calcined in a tube furnace at 450 °C in N_2 for 6 h to obtain porous MnO/C. The sketch of the T-shaped microchannel reactor is depicted in Fig. 1(b). The microchannel reactor has a mixing channel length of 50 mm, a width of 0.8 mm and a depth of 0.2 mm, while each inlet channels have widths of 0.4 mm and lengths of 10 mm. During the experiments, two opposite feed streams, $MnSO_4$ and NH_4HCO_3 solutions, mixed at the crunode, where the reactants impinge, flow through the vertical channel as the reaction proceeds.

2.2. Characterization of Materials

The crystalline structure and phase information of the as-prepared products were determined by X-ray powder diffraction (XRD) on an X' Pert PRO X-ray diffractometer (D8, Bruker, Germany) with Cu-Kα radiation (V = 40 KV, I = 40 mA and λ = 0.15406 nm) in the range of 10–80°. The morphology and particle sizes of the resultant samples were characterized with a field emission scanning electron microscope (FE

Peer-reviewed version available at Nanomaterials 2017, 7, , 121; doi:10.3390/nano7060121

SEM, Hitachi S-3400, Japan) and a transmission electron microscope (FE TEM, Tecnai G2 F20, USA). The nitrogen adsorption-desorption isotherms were measured on a V-Sorb 2800 series analyzer (Gold APP Instruments, China) to calculate the specific area by the Brunauer–Emmett–Teller (BET) analysis method and the pore size distribution by the Barrett–Joyner–Halenda method. The carbon content in the final product was tested using a Flash2000 elemental analyzer (Thermo Fisher Scientific, USA).

2.3. Electrochemical measurements

The electrochemical performance of MnO/C was tested using CR2032 coin-type half cells. The working electrode was produced by mixing MnO/C, acetylene black, and a lithium polyacrylate (Li-PAA) binder [40] in a weight ratio of 8:1:1, in distilled water to form a homogenous slurry. The slurry mixture was coated on a copper foil substrate, followed by drying at 120 °C in a vacuum oven for 12 h. Half Li-ion battery cells were assembled in a glove-box filled with a dry and high purity argon atmosphere. The coins use lithium metal foils as the counter/reference electrode, a Celgard 2300 as the separator, and 1 $mol \cdot L^{-1}$ $LiPF_6$ (dissolved in ethylene carbonate and dimethyl carbonate with a volume ratio of 1:1) as the electrolyte. The galvanostatic charge and discharge measurements of the cells were evaluated on NEWARE BTS battery

cycler (Shenzhen, China) at different current densities in a voltage range from 0.01 to 3 V. The charge/discharge current density and the specific capacity were calculated based on the whole weight of MnO/C in the electrode, where a 1 C rate was 755 $mAh \cdot g^{-1}$. Cyclic voltammogram (CV) measurements were conducted on a PCI 4750 electrochemical workstation(Gamry, USA) with a scan rate of 0.1 $mV \cdot s^{-1}$ and potential windows ranging from 0.01 to 3 V (versus Li/Li^{+}). Electrochemical impedance spectroscopy (EIS) was completed using a Gamry PCI-4750 electrochemical workstation in a frequency range from 100 kHz to 1 mHz.

3. Results and discussion

3.1. Characterization of Samples

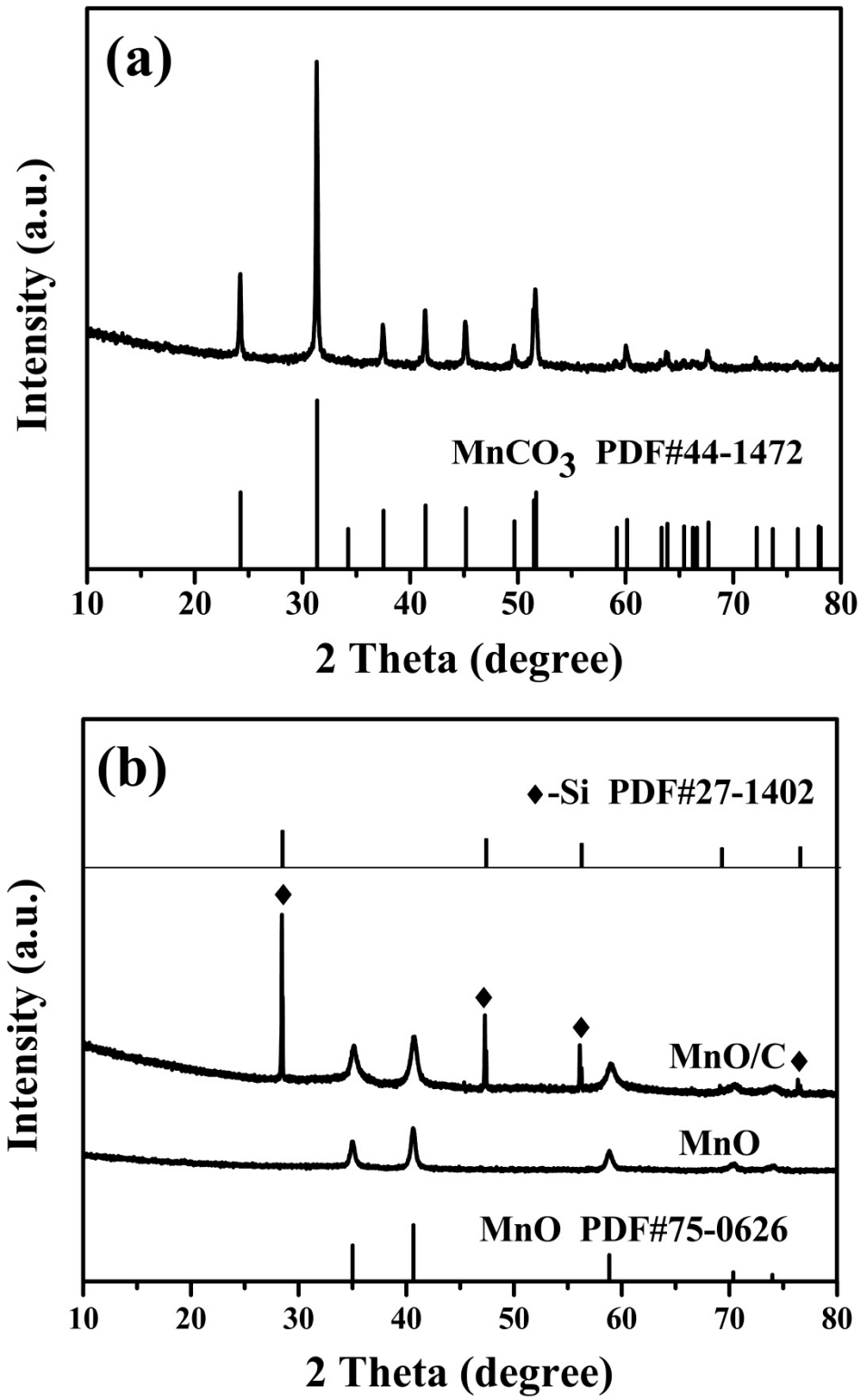

Fig.2. XRD patterns of $MnCO_3$ precursor (a) and the calcined $MnCO_3$ (b) (the top is MnO/C sample; the bottom is MnO sample)

The XRD patterns of the $MnCO_3$ precursor are shown in Fig. 2(a). All diffraction peaks agree perfectly with the rhombohedral $MnCO_3$ structure (JCPDS 44-1472) and no other phases were detected, indicating the high purity $MnCO_3$ precursor had been prepared by the T-type microchannel reactor. The XRD characteristic peaks of the pure phase MnO and MnO/C composites are presented in Fig. 2(b). All the peaks of the products were coincident with the standard XRD pattern of cubic MnO (JCPDS 75-0626) and no impure diffraction peaks were observed, confirming that $MnCO_3$ had been completely decomposed into MnO without generation of any other substance, and the carbon layer formed on the MnO surface was amorphous. The lattice constants of the MnO/C phase were calculated as a = b = c = 4.434(1) Å, V = 87.18 Å, and $\alpha = \beta = \gamma = 90°$, which coincided well with the literature [41–43].

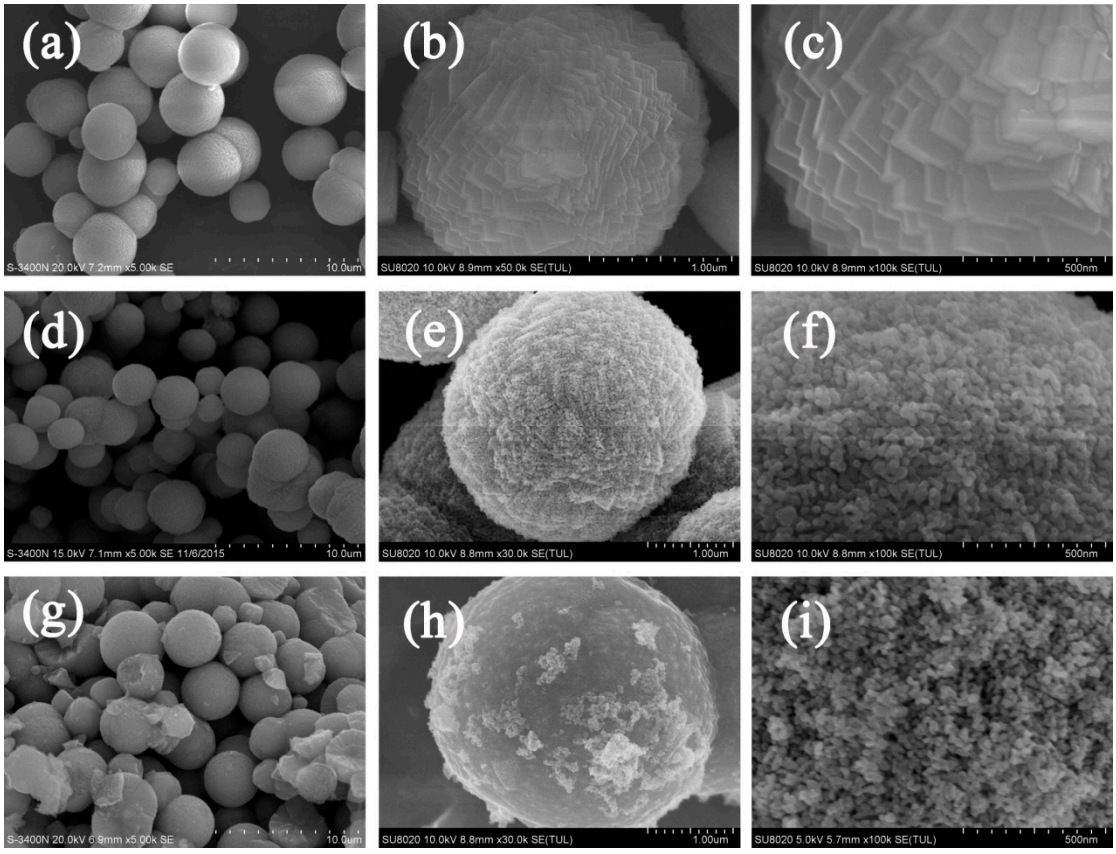

Fig. 3. FE-SEM images of $MnCO_3$ (a, b and c), MnO (d, e and f), MnO/C (g, h and i).

Fig. 3(a)-3(c) present the SEM images of the prepared $MnCO_3$ microspheres with approximate sizes distribution of 2-3 μm, and the surface of microspheres is consisted of flake-like particles with a thickness about 50 nm. Compared to $MnCO_3$ prepared in bulk batch reactors [35], our microchannel reactor can develop $MnCO_3$ with a smaller mean particle size may due to better mixing effect and improved mass transfer performance in the microfluidic device [44]. The Reynolds number for the feed channel was 2781 when the flow rate was 50 $mL \cdot min^{-1}$ (H_2O in 10 °C was used as the flow media), which is much larger than the 1110 that reported for a similar microchannel reactor [45].

The impinging of liquid with a high velocity and a large Reynolds number at the T-junction induced a high intensity vortex, which led to efficient micromixing and preparation of the $MnCO_3$ microspheres.

The SEM images in Figs. 3(d) and 3(g) demonstrated the morphological characteristics of MnO and MnO/C, no apparent variations of spherical structure during the calcination process. Figs. 3(e), 3(f), 3(h), and 3(i) show that the surface of MnO/C is glossier than MnO, on account of the formation of the carbon stratum. The inner morphology of MnO/C is the same as MnO, with both being composed of loosely packed primary particles with diameters of about 50 nm and tiny porous structures which were generated by CO_2 release during calcination. However, the emancipating CO_2 also caused volume expansion that led to an increase in the particle sizes of MnO and MnO/C, which had proximate diameters of 3–4 μm.

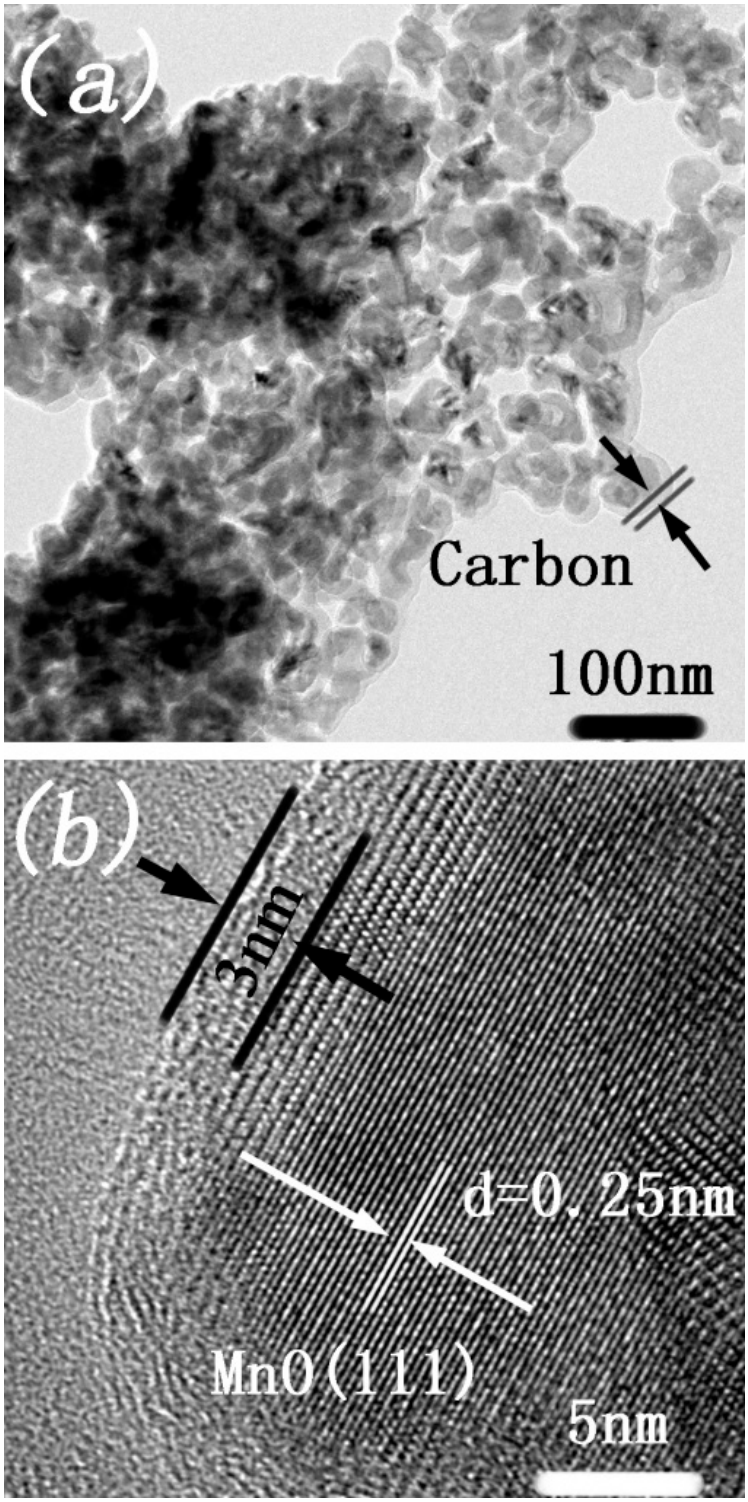

Fig. 4. FE-TEM images of MnO/C microspheres.

The FE TEM images of the MnO/C microspheres are exhibited in Fig. 4(a). The prepared MnO/C microspheres were composed of nano-sized

grains, and the voids between the nanoparticles form a porous framework. The HRTEM image in Fig. 4(b) shows a continuous and uniform carbon layer (about 3–4 nm) along the MnO surface and the carbon content of the final sample was 21.92%. This clearly demonstrated that the lattice fringe spacing is about 0.25 nm, corresponding to the cubic MnO XRD results for the (111) crystal plane.

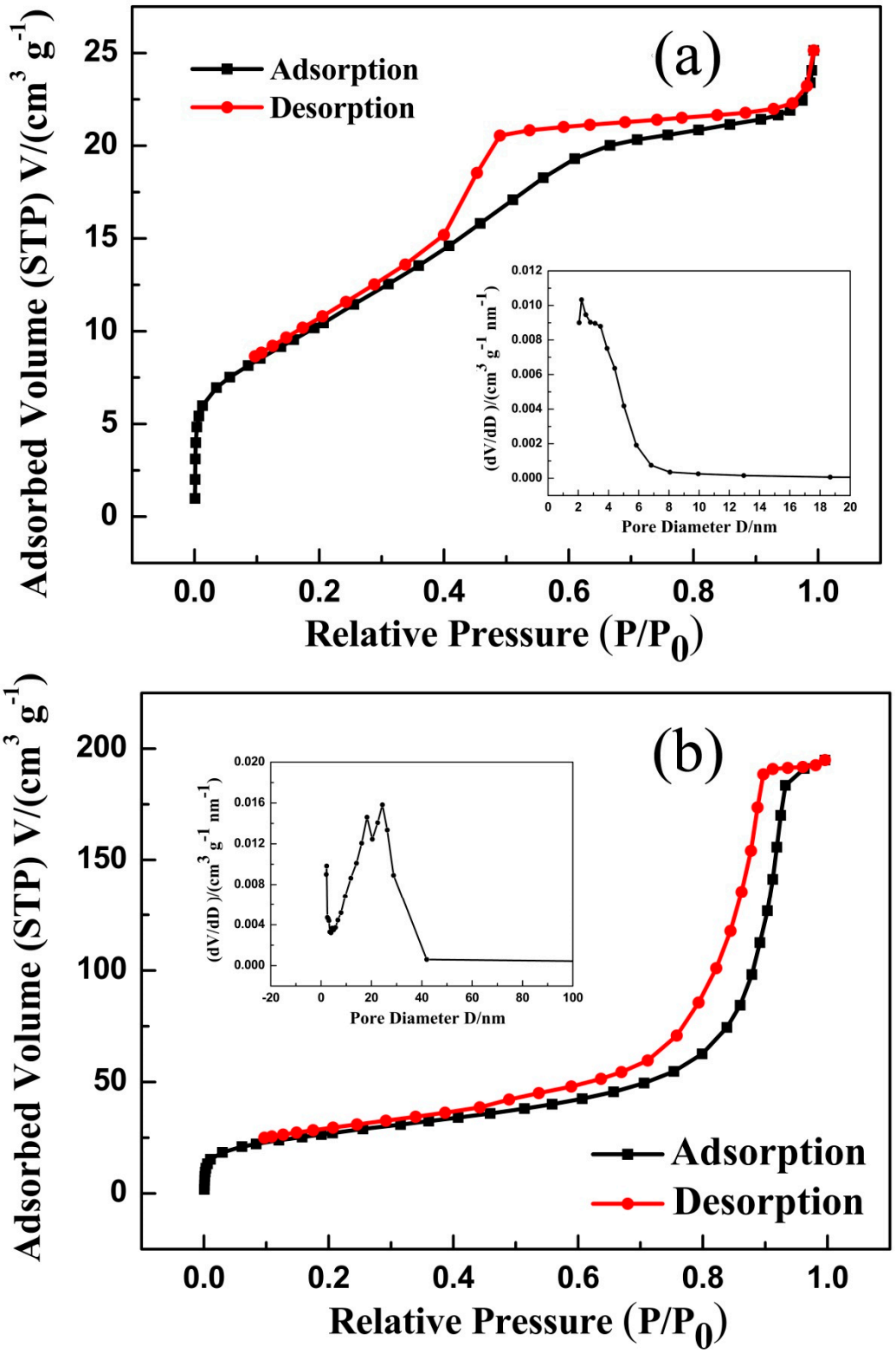

Fig. 5. N_2 adsorption-desorption isotherms of $MnCO_3$ (a) and MnO/C (b). The insets show the two samples of the pore-size distributions.

The BET specific surface areas and porous structures of $MnCO_3$ and

MnO/C were further measured by nitrogen adsorption-desorption isotherms. Fig. 5 shows the isotherms and pore size distribution of the two specimens. The isotherm of $MnCO_3$ exhibits type IV isotherm behavior with obvious H2 hysteresis loops and MnO/C displays typical IV isotherms with H3 hysteresis loops, both of the samples confirm the presence of mesopores. From the inset of Fig. 5(a), the average pore size of $MnCO_3$ is 2.22 nm and the BET surface area is measured to be 38.06 $m^2 \cdot g^{-1}$. The corresponding pore size distribution of MnO/C is clarified in the inset of Fig. 5(b), with an average pore size of 24.37 nm in diameter, in accordance with the FE SEM and TEM images, and a BET specific surface area of 96.66 $m^2 \cdot g^{-1}$. The BET surface area and the pore size of MnO/C are larger than $MnCO_3$ which is mainly attributed to the release of CO_2 during the decomposition of $MnCO_3$. In addition, such a porous structure, with a higher specific surface area than in previous studies [31, 41, 46, 47], can not only accelerate the diffusion of Li^+ between the electrolyte and internal active materials, but also buffer the volume variation during Li^+ insertion/extraction to promote the reversible capacity and the stability of the cycling performance [46, 48].

3.2. Electrochemical performance of MnO/C electrode

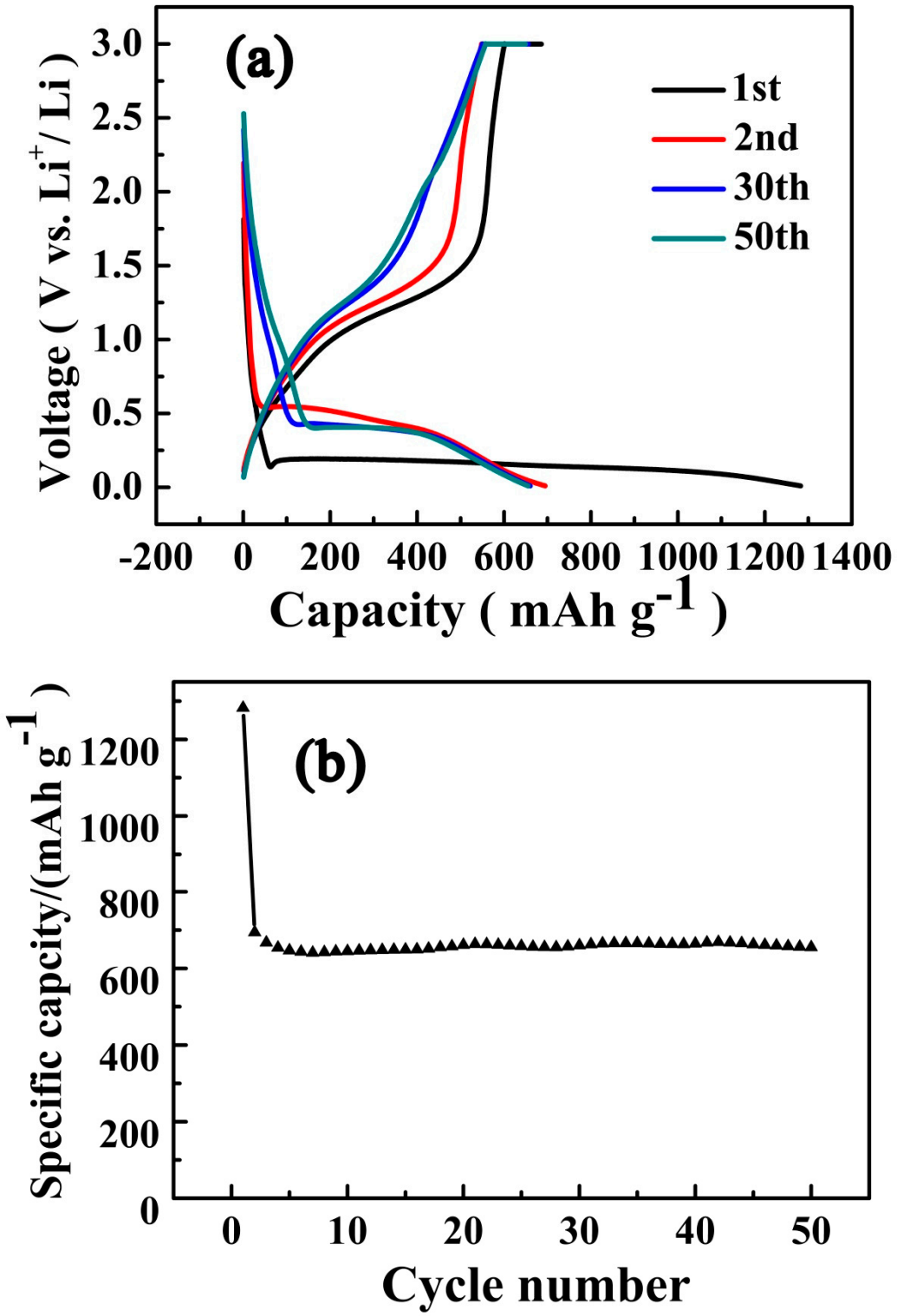

Fig. 6. Charge-discharge curves (a) and cycling performance (b) of the prepared MnO/C sample at a rate of 1C

To examine the electrochemical storage properties of the as-prepared porous MnO/C material, galvanostatic discharge-charge cycling was firstly explored, as shown in Fig. 6. The initial and second discharge specific capacities of the MnO/C sample at 1 C (755 $mA \cdot g^{-1}$) were 1282.3 and 694.4 $mAh \cdot g^{-1}$, respectively. The first discharge capacity was much higher than the theoretical value (755 $mAh \cdot g^{-1}$) The irreversible capacity loss in the first cycle was mainly attributed to the formation of the solid electrolyte interface (SEI) layer and to a certain extent, decomposition of the electrolyte [33, 36, 49, 50]. However, from the second cycle, the MnO/C electrodes exhibit excellent cycling performance, accompanied with Coulombic efficiency which was maintained at almost 100%. The first discharge voltage plateau at 0.1 V in Fig 6(a) is corresponded to the initial reduction of MnO to Mn and the formation of the SEI layer [23, 33, 51], then the discharge plateau turned to 0.3 V in the subsequent cycles, indicating the irreversible phase transformation, owing to the formation of Li_2O and metallic Mn [7, 47, 52]. The charge curves show no voltage plateau, but a slope from 1.0 to 1.5 V, suggesting the oxidation of Mn to MnO [13, 15, 47]. From Fig. 6(b), we discover that the discharge specific capacity after 50 cycles can still be retained as high as 654.8 $mAh \cdot g^{-1}$ with a capacity retention rate of 98%, except for the initial two cycles, thus exhibiting excellent electrochemical properties compared with the MnO/C prepared by the

traditional co-precipitation method [22, 35].

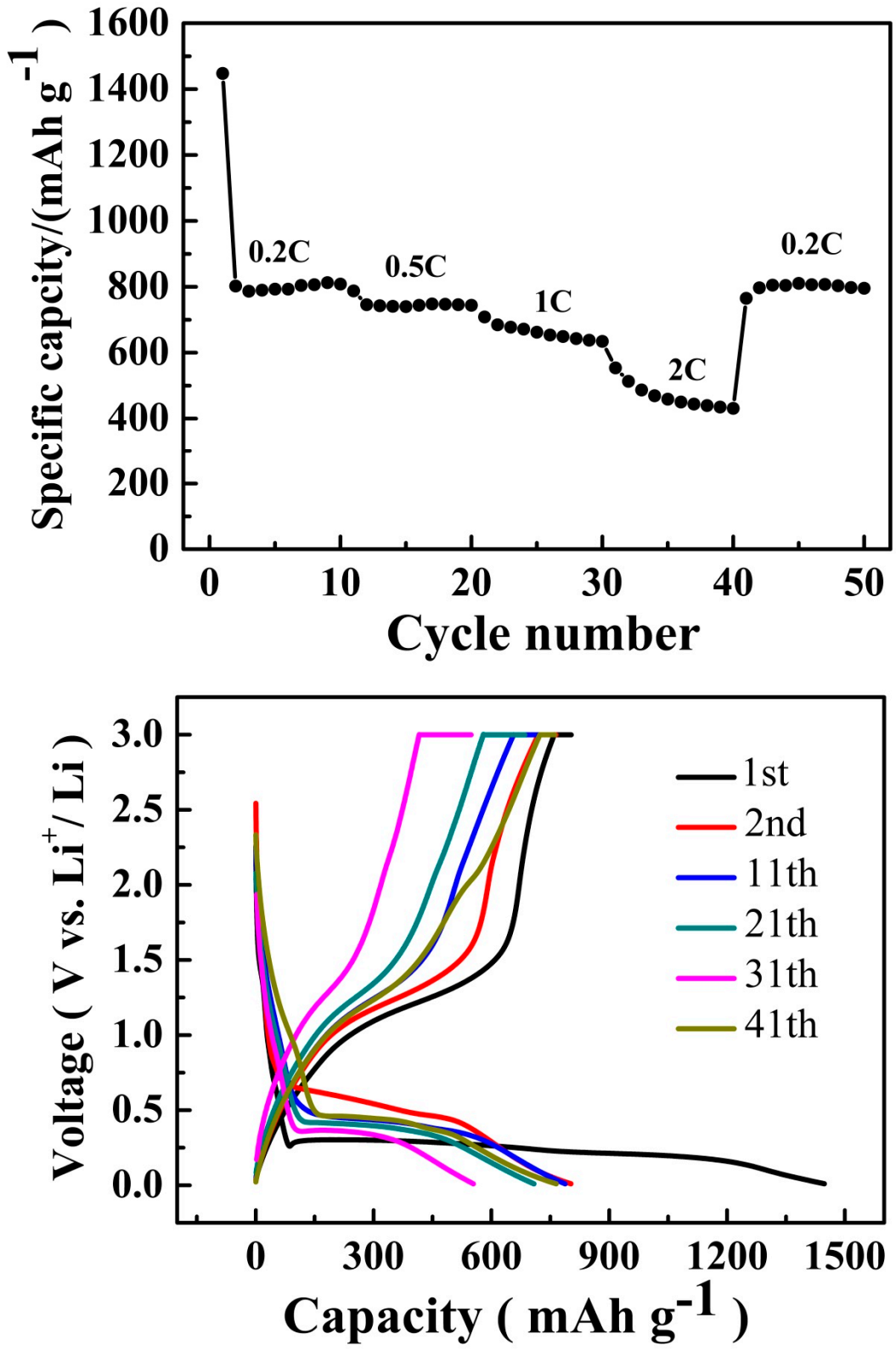

Fig. 7. Rate performances (a) and galvanostatic discharge/charge profiles

(b) of the porous MnO/C at various current rates

The rate capacities of the porous MnO/C microspheres at various current densities are exhibited in Fig. 7. The corresponding discharge capacities reach 808.3, 743.7, 642.6, 450.1, and 803.1 $mAh \cdot g^{-1}$ at 0.2, 0.5, 1, 2, and 0.2 C, respectively. It is worth noting that when the current density was decreased back to 0.2 C, the discharge capacity of 803.1 $mAh \cdot g^{-1}$ was almost 100% recovered, illustrating the excellent rate capability and structural stability. The outstanding electrochemical performance of MnO/C is mainly attributed to the porous structure with a high specific surface area and the carbon coating, which can effectively accommodate the stress and strain of volume change and hinder the agglomeration and separation of MnO during the Li-ion insertion/extraction process. In comparison with the traditional co-precipitation method [9, 22–24, 30, 35], our method not only presents a sample with remarkable specific capacity, significant cycling stability, and excellent rate performance, but also shortens the reaction time, strengthens the mixing effect, and makes it is easy to control the reaction process. Clearly, these results indicate that our T-shaped microchannel reactor method is a very promising method for synthesizing high-performance MnO/C and related materials.

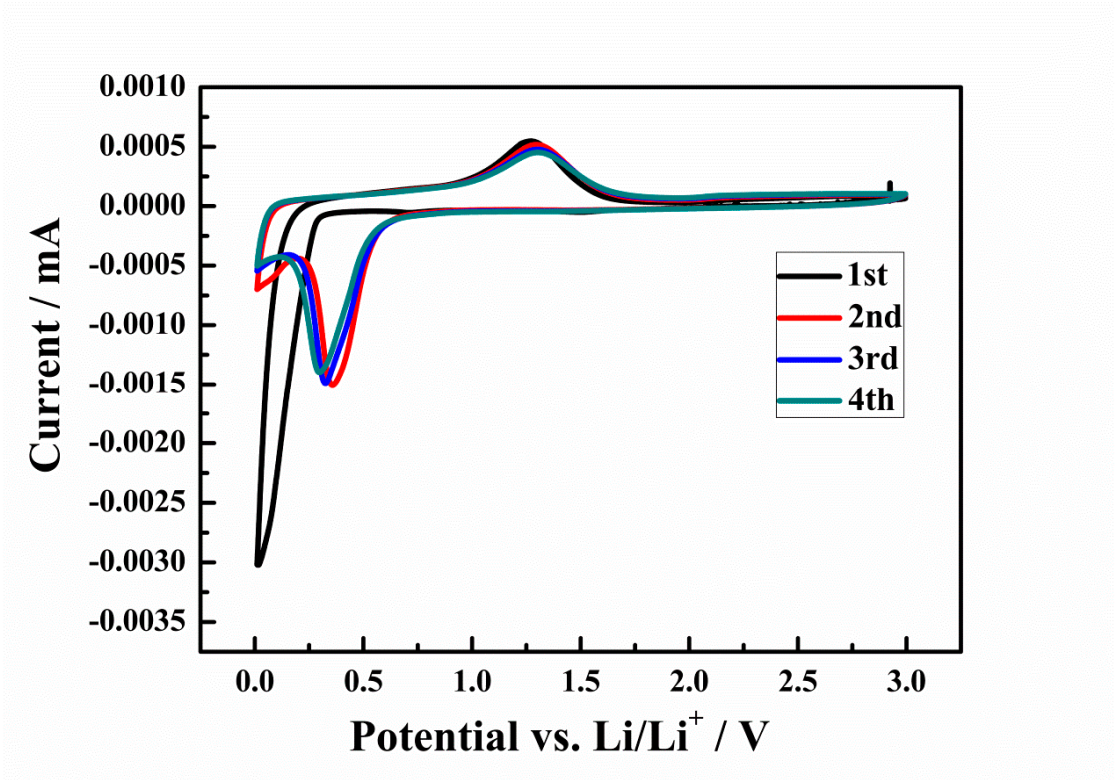

Fig. 8. CV curves of the porous MnO/C at a scan rate of 0.1 $mV \cdot s^{-1}$

The CV curves of the porous MnO/C composite electrode in a voltage range from 0.01–3.0 V with a scan rate of 0.1 $mV \cdot s^{-1}$ for the first four cycles are shown in Fig. 8. In the first cathodic sweep, only one sharp reduction peak close to 0.1 V is observed, agreeing well with the shaping of the SEI layers and the reduction of Mn^{2+} to Mn^0. From the second cycle onwards, the main reduction current peak turns to 0.3 V, suggesting the formation of Li_2O and metallic Mn, presented as $MnO + 2\ Li \rightarrow Mn^0 + Li_2O$, which is an irreversible phase transformation [28, 3]. In the oxidation half cycle, a wide main peak is observed at 1.3 V, in good accord with the oxidation of Mn^0 to Mn^{2+} and the decomposition of Li_2O [30, 37, 53]. Both the reduction and oxidation curves in the subsequent cycles overlap well, demonstrating the excellent reversibility of the

Preprints (www.preprints.org) | NOT PEER-REVIEWED | Posted: 11 May 2017 doi:10.20944/preprints201705.0094.v1

Peer-reviewed version available at Nanomaterials 2017, 7, , 121; doi:10.3390/nano7060121

electrochemical reaction, which matches well with the charge/discharge experiments.

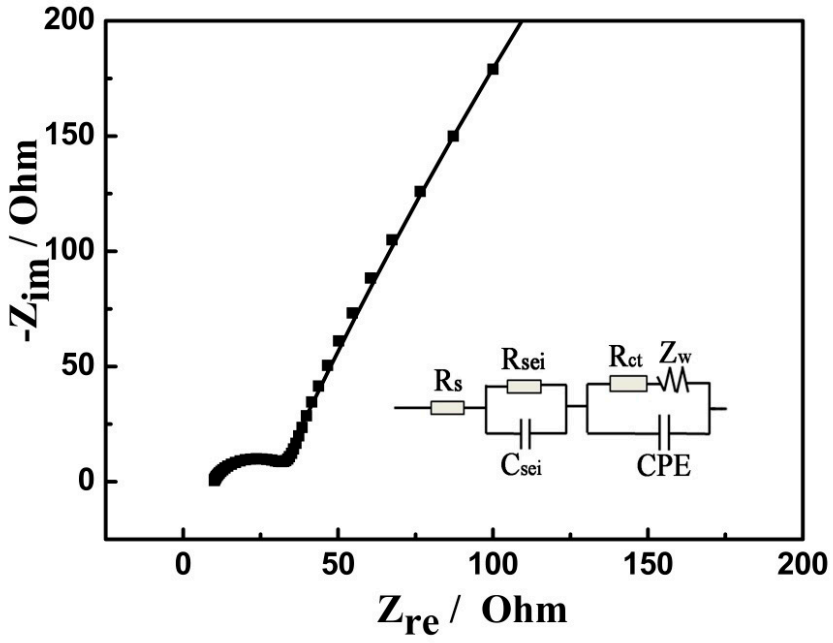

Fig. 9. Impendence spectra for the prepared porous MnO/C

EIS was further executed to explore the electrochemical characteristics of the electrode/electrolyte interface. Fig. 9 shows the Nyquist plot of the MnO/C electrode without any discharge/charge cycles, and the inset gives an equivalent circuit of impendence spectra. The intercept of the high-frequency semicircle on the Z' axis is ascribed to the resistance of the electrolyte (R_s). The high-frequency semicircle is associated with the capacitance (C_{sei}) and the resistance (R_{sei}) of the SEI layer. The middle-frequency semicircle is attributed to the charge transfer resistance (R_{ct}) between the electrode. The straight line in low frequency is consistent with Warburg impendence (Z_w), corresponding to the diffusion

Peer-reviewed version available at Nanomaterials 2017, 7, , 121; doi:10.3390/nano7060121

of Li-ions into the bulk electrode [33, 42]. The fitting values of kinetic parameters of MnO/C electrode are listed in Table 1. It is worth noting that the R_{ct} is much lower than that previously reported [13, 22], indicating much higher reaction areas and faster charge transfer at the electrode/electrolyte interface [9, 33], which is contributed to by the high surface area of the mesoporous structure and the carbon coating which facilitates the charge-transfer reaction. The diffusion coefficient of lithium ions (D_{Li}) in the MnO/C sample is 3.64×10^{-18} $cm^2\cdot s^{-1}$, which is larger than that reported by Yang et al. [18]. These results further illustrate that the porous MnO/C microspheres should display excellent electrochemistry performance.

Table 1. Simulation results of EIS in Fig. 9.

R_s /Ω	C_{sei} /F cm^{-2}	R_{sei} /Ω	CPE Y_o /S s^n cm^{-2}	R_{ct} /Ω	Z_w /S $s^{0.5}$ cm^{-2}
3.88	6.45×10^{-5}	23.62	3.36×10^{-4}	16.32	0.00889

4. Conclusions

In this work, we demonstrated a novel, economic and facile strategy for fabricating porous MnO/C microspheres by employing a T-shaped microchannel reactor. The resulting porous MnO/C microspheres had an average pore size of 24.37 nm and a larger specific surface area of 96.66 $m^2\cdot g^{-1}$. As anode materials for Li-ion batteries, the prepared porous MnO/C microspheres demonstrated electrochemical performance with a

discharge capacity of 655.4 $mAh \cdot g^{-1}$ at 1 C after 50 cycles, which is mainly ascribed to the mesoporous structure and the carbon coating which stimulated Li-ion diffusion into the cathode, by increasing the electrochemical reaction surface and accommodating the volumes changes in the electrochemical reactions. The approach used in this work provided a fast, easily controllable and mass-production way to fabricate porous MnO/C composites, which can dramatically save time and cost.

Acknowledgements

The authors appreciate financial support from the National Natural Science Foundation of China (51564002) and the Guangxi Postdoctoral Foundation.

Author Contributions

Jing Su and Hao Liang performed the experiments, analyzed the data and drafted the manuscript. Xian-Nian Gong, Xiao-Yan Lv and Yun-Fei Long contributed to the idea and discussion of the manuscript. Yan-Xuan Wen as the PI of this research contributed to the idea, discussion and writing of the final manuscript.

References

[1] Etacheri, V.; Marom, R.; Elazari, R.; Salitra, G.; Aurbach, D. Challenges in the development of advanced Li-ion batteries: a review. *ENERG ENVIRON SCI* **2011**, 4, 3243-3262.

[2] Goodenough, J.B.; Park, K. The Li-Ion Rechargeable Battery: A Perspective. *J AM CHEM SOC* **2013**, 135, 1167-1176.

[3] Cho, J.S.; Hong, Y.J.; Kang, Y.C. Design and Synthesis of Bubble-Nanorod-Structured Fe2O3-Carbon Nanofibers as Advanced Anode Material for Li-Ion Batteries. *ACS NANO* **2015**, 9, 4026-4035.

[4] Wang, J.; Zhang, C.; Kang, F. Nitrogen-Enriched Porous Carbon Coating for Manganese Oxide Nanostructures toward High-Performance Lithium-Ion Batteries. *ACS APPL MATER INTER* **2015**, 7, 9185-9194.

[5] Wang, J.; Yang, Y.; Huang, Z.; Kang, F. MnO-carbon hybrid nanofiber composites as superior anode materials for lithium-ion batteries. *ELECTROCHIM ACTA* **2015**, 170, 164-170.

[6] Lee, R.; Lin, Y.; Weng, Y.; Pan, H.; Lee, J.; Wu, N. Synthesis of high-performance MnOx/carbon composite as lithium-ion battery anode by a facile co-precipitation method: Effects of oxygen stoichiometry and carbon morphology. *J POWER SOURCES* **2014**, 253, 373-380.

[7] Li, X.; Zhu, Y.; Zhang, X.; Liang, J.; Qian, Y. MnO@1-D carbon composites from the precursor C4H4MnO6 and their high-performance in lithium batteries. *RSC ADV* **2013**, 3, 10001-10006.

[8] Guo, J.; Liu, Q.; Wang, C.; Zachariah, M.R. Interdispersed Amorphous MnOx-Carbon Nanocomposites with Superior Electrochemical Performance as Lithium-Storage Material. *ADV FUNCT MATER* **2012**, 22, 803-811.

[9] Wang, S.; Xing, Y.; Xu, H.; Zhang, S. MnO Nanoparticles Interdispersed in 3D Porous Carbon Framework for High Performance Lithium-Ion Batteries. *ACS APPL MATER INTER* **2014**, 6, 12713-12718.

[10] Qiao, H.; Yao, D.; Cai, Y.; Huang, F.; Wei, Q. One-pot synthesis and electrochemical property of MnO/C hybrid microspheres. *IONICS* **2013**, 19, 595-600.

[11] Sun, Y.; Hu, X.; Luo, W.; Xia, F.; Huang, Y. Reconstruction of Conformal Nanoscale MnO on Graphene as a High-Capacity and Long-Life Anode Material for Lithium Ion Batteries. *ADV FUNCT MATER* **2013**, 23, 2436-2444.

[12] Zhang, S.; He, W.; Zhang, X.; Yang, X. Rational design of carbon-coated hollow MnO nanotubes for Li-ion batteries. *J MATER SCI-MATER EL* **2015**, 26, 2189-2197.

[13] Yang, C.; Gao, Q.; Tian, W.; Tan, Y.; Zhang, T.; Yang, K.; Zhu, L. Superlow load of nanosized MnO on a porous carbon matrix from wood fibre with superior lithium ion storage performance. *J MATER CHEM A* **2014**, 2, 19975-19982.

[14] Liu, B.; Hu, X.; Xu, H.; Luo, W.; Sun, Y.; Huang, Y. Encapsulation of MnO Nanocrystals in Electrospun Carbon Nanofibers as High-Performance Anode Materials for Lithium-Ion Batteries. *SCI REP-UK* **2014**, 4.

[15] Hu, H.; Cheng, H.; Liu, Z.; Yu, Y. Facile Synthesis of Carbon Spheres with Uniformly Dispersed MnO Nanoparticles for Lithium Ion Battery Anode. *ELECTROCHIM ACTA* **2015**, 152, 44-52.

[16] Wang, S.; Ren, Y.; Liu, G.; Xing, Y.; Zhang, S. Peanut-like MnO@C core-shell composites as anode electrodes for high-performance lithium ion batteries. *NANOSCALE* **2014**, 6, 3508-3512.

[17] Zhang, X.; Xing, Z.; Wang, L.; Zhu, Y.; Li, Q.; Liang, J.; Yu, Y.; Huang, T.; Tang, K.; Qian, Y.; et al. Synthesis of MnO@C core-shell nanoplates with controllable shell thickness and their electrochemical performance for lithium-ion batteries. *JOURNAL OF MATERIALS CHEMISTRY* **2012**, 22, 17864-17869.

[18] Chen, W.; Qie, L.; Shen, Y.; Sun, Y.; Yuan, L.; Hu, X.; Zhang, W.; Huang, Y. Superior lithium storage performance in nanoscaled MnO promoted by N-doped carbon webs. *NANO ENERGY* **2013**, 2, 412-418.

[19] Gu, X.; Yue, J.; Chen, L.; Liu, S.; Xu, H.; Yang, J.; Qian, Y.; Zhao, X. Coaxial MnO/N-doped carbon nanorods for advanced lithium-ion battery anodes. *J MATER CHEM A* **2015**, 3, 1037-1041.

[20] Masai, H.; Hino, Y.; Yanagida, T.; Fujimoto, Y. Photoluminescence and radioluminescence properties of MnO-doped SnO-ZnO-P2O5 glasses. *OPT MATER* **2015**, 42, 381-384.

[21] Chen, R.; Yan, J.; Liu, Y.; Li, J. Three-Dimensional Nitrogen-Doped Graphene/MnO Nanoparticle Hybrids as a High-Performance Catalyst for Oxygen Reduction Reaction. *J PHYS CHEM C* **2015**, 119, 8032-8037.

[22] Sun, X.; Xu, Y.; Ding, P.; Chen, G.; Zheng, X.; Zhang, R.; Li, L. The composite sphere of manganese oxide and carbon nanotubes as a prospective anode material for lithium-ion batteries. *J POWER SOURCES* **2014**, 255, 163-169.

[23] Mai, Y.J.; Zhang, D.; Qiao, Y.Q.; Gu, C.D.; Wang, X.L.; Tu, J.P. MnO/reduced graphene oxide sheet hybrid as an anode for Li-ion batteries with enhanced lithium storage performance. *J POWER SOURCES* **2012**, 216, 201-207.

[24] Liu, Y.; Zhao, X.; Li, F.; Xia, D. Facile synthesis of MnO/C anode materials for lithium-ion batteries. *ELECTROCHIM ACTA* **2011**, 56, 6448-6452.

[25] Su, L.; Zhong, Y.; Wei, J.; Zhou, Z. Preparation and electrochemical Li storage performance of MnO@C nanorods consisting of ultra small MnO nanocrystals. *RSC ADV* **2013**, 3, 9035-9041.

[26] Zhu, C.; Sheng, N.; Akiyama, T. MnO nanoparticles embedded in a carbon matrix for a high performance Li ion battery anode. *RSC ADV* **2015**, 5, 21066-21073.

[27] Jiang, H.; Hu, Y.; Guo, S.; Yan, C.; Lee, P.S.; Li, C. Rational Design of MnO/Carbon Nanopeapods with Internal Void Space for High-Rate and Long-Life Li-Ion Batteries. *ACS NANO* **2014**, 8, 6038-6046.

[28] Li, X.; Li, D.; Qiao, L.; Wang, X.; Sun, X.; Wang, P.; He, D. Interconnected porous MnO nanoflakes for high-performance lithium ion battery anodes. *JOURNAL OF MATERIALS CHEMISTRY* **2012**, 22, 9189-9194.

[29] Xu, G.; Xu, Y.; Sun, H.; Fu, F.; Zheng, X.; Huang, L.; Li, J.; Yang, S.; Sun, S. Facile synthesis of porous MnO/C nanotubes as a high capacity anode material for lithium ion batteries. *CHEM COMMUN* **2012**, 48, 8502-8504.

[30] Wang, X.; Qiu, S.; Lu, G.; He, C.; Liu, J.; Luan, L.; Liu, W. Fabrication of porous MnO microspheres with carbon coating for lithium ion battery application. *CRYSTENGCOMM* **2014**, 16, 1802-1809.

[31] Li, X.; Shang, X.; Li, D.; Yue, H.; Wang, S.; Qiao, L.; He, D. Facile Synthesis of Porous MnO Microspheres for High-Performance Lithium-Ion Batteries. *PART PART SYST CHAR* **2014**, 31, 1001-1007.

[32] Yue, J.; Gu, X.; Chen, L.; Wang, N.; Jiang, X.; Xu, H.; Yang, J.; Qian, Y. General synthesis of hollow MnO2, Mn3O4 and MnO nanospheres as superior anode materials for lithium ion batteries. *J MATER CHEM A* **2014**, 2, 17421-17426.

[33] Xia, Y.; Xiao, Z.; Dou, X.; Huang, H.; Lu, X.; Yan, R.; Gan, Y.; Zhu, W.; Tu, J.; Zhang, W.; et al. Green and Facile Fabrication of Hollow Porous MnO/C Microspheres from Microalgaes for Lithium-Ion Batteries. *ACS NANO* **2013**, 7, 7083-7092.

[34] Anh, V.; Qian, Y.; Stein, A. Porous Electrode Materials for Lithium-Ion Batteries - How to

Prepare Them and What Makes Them Special. *ADV ENERGY MATER* **2012**, 2, 1056-1085.

[35] Zhong, K.; Zhang, B.; Luo, S.; Wen, W.; Li, H.; Huang, X.; Chen, L. Investigation on porous MnO microsphere anode for lithium ion batteries. *J POWER SOURCES* **2011**, 196, 6802-6808.

[36] Guo, S.; Lu, G.; Qiu, S.; Liu, J.; Wang, X.; He, C.; Wei, H.; Yan, X.; Guo, Z. Carbon-coated MnO microparticulate porous nanocomposites serving as anode materials with enhanced electrochemical performances. *NANO ENERGY* **2014**, 9, 41-49.

[37] Ma, X.; Wan, Q.; Huang, X.; Ding, C.; Jin, Y.; Guan, Y.; Chen, C. Synthesis of three-dimensionally porous MnO thin films for lithium-ion batteries by improved Electrostatic Spray Deposition technique. *ELECTROCHIM ACTA* **2014**, 121, 15-20.

[38] Liang, Y.; Chu, G.; Wang, J.; Huang, Y.; Chen, J.; Sun, B.; Shao, L. Controllable preparation of nano-CaCO3 in a microporous tube-in-tube microchannel reactor. *CHEM ENG PROCESS* **2014**, 79, 34-39.

[39] Li, S.; Xu, H.; Wang, Y.; Luo, G. Controllable preparation of nanoparticles by drops and plugs flow in a microchannel device. *LANGMUIR* **2008**, 24, 4194-4199.

[40] Li, J.; Le, D.; Ferguson, P.P.; Dahn, J.R. Lithium polyacrylate as a binder for tin-cobalt-carbon negative electrodes in lithium-ion batteries. *ELECTROCHIM ACTA* **2010**, 55, 2991-2995.

[41] Sun, Y.; Hu, X.; Luo, W.; Huang, Y. Porous carbon-modified MnO disks prepared by a microwave-polyol process and their superior lithium-ion storage properties. *JOURNAL OF MATERIALS CHEMISTRY* **2012**, 22, 19190-19195.

[42] Sun, X.; Xu, Y.; Ding, P.; Chen, G.; Zheng, X. Superior lithium storage of the carbon modified hybrid of manganese monoxide and carbon nanotubes. *MATER LETT* **2013**, 113,

186-189.

[43] Sun, X.; Xu, Y.; Ding, P.; Jia, M.; Ceder, G. The composite rods of MnO and multi-walled carbon nanotubes as anode materials for lithium ion batteries. *J POWER SOURCES* **2013**, 244, 690-694.

[44] Zhao, C.; He, L.; Qiao, S.Z.; Middelberg, A.P.J. Nanoparticle synthesis in microreactors. *CHEM ENG SCI* **2011**, 66, 1463-1479.

[45] Ying, Y.; Chen, G.; Zhao, Y.; Li, S.; Yuan, Q. A high throughput methodology for continuous preparation of monodispersed nanocrystals in microfluidic reactors. *CHEM ENG J* **2008**, 135, 209-215.

[46] Luo, W.; Hu, X.; Sun, Y.; Huang, Y. Controlled Synthesis of Mesoporous MnO/C Networks by Microwave Irradiation and Their Enhanced Lithium-Storage Properties. *ACS APPL MATER INTER* **2013**, 5, 1997-2003.

[47] Wang, T.; Peng, Z.; Wang, Y.; Tang, J.; Zheng, G. MnO Nanoparticle@Mesoporous Carbon Composites Grown on Conducting Substrates Featuring High-performance Lithium-ion Battery, Supercapacitor and Sensor. *SCI REP-UK* **2013**, 3.

[48] Su, K.; Wang, C.; Nie, H.; Guan, Y.; Liu, F.; Chen, J. Facile template-free synthesis of 3D porous MnO/C microspheres with controllable pore size for high-performance lithium-ion battery anodes. *J MATER CHEM A* **2014**, 2, 10000-10006.

[49] Zhang, J.; Yang, X.; Wang, R.; Dong, W.; Lu, W.; Wu, X.; Wang, X.; Li, H.; Chen, L. Influences of Additives on the Formation of a Solid Electrolyte Interphase on MnO Electrode Studied by Atomic Force Microscopy and Force Spectroscopy. *J PHYS CHEM C* **2014**, 118, 20756-20762.

[50] Tao, X.; Chai, W.; Xu, F.; Luo, J.; Xiao, H.; Liang, C.; Gan, Y.; Huang, H.; Xia, Y.; Zhang, W. Bio-templated Fabrication of Highly Defective Carbon Anchored MnO Anode Materials with High Reversible Capacity. *ELECTROCHIM ACTA* **2015**, 169, 159-167.

[51] Wang, S.; Xiao, C.; Xing, Y.; Xu, H.; Zhang, S. Formation of a stable carbon framework in a MnO yolk-shell sphere to achieve exceptional performance for a Li-ion battery anode. *J MATER CHEM A* **2015**, 3, 15591-15597.

[52] Sun, B.; Chen, Z.; Kim, H.; Ahn, H.; Wang, G. MnO/C core-shell nanorods as high capacity anode materials for lithium-ion batteries. *J POWER SOURCES* **2011**, 196, 3346-3349.

[53] Xu, S.; Zhu, Y.; Zhuang, Q.; Wu, C. Hydrothermal synthesis of manganese oxides/carbon nanotubes composites as anode materials for lithium ion batteries. *MATER RES BULL* **2013**, 48, 3479-3484.